Fabrication and Applications of In-Fiber Semiconductor and Metal Microspheres

By

Tara Sarathi

B.S. Materials Science and Engineering,
Massachusetts Institute of Technology, Cambridge, MA, 2012

Submitted to the Department of Materials Science and Engineering in partial fulfillment of the requirements for the degree of

Masters of Science in Materials Science and Engineering

at the

MASSACHUSETTS INSTITUTE OF TECHNOLOGY

February 2015

© Massachusetts Institute of Technology 2015. All rights reserved.

Author_____
Department of Materials Science and Engineering
December 15, 2014

Certified by_____
Yoel Fink
Professor of Materials Science
Professor of Electrical Engineering and Computer Science
Thesis Supervisor

Accepted by_____
Donald Sadoway
Chair, Departmental Committee on Graduate Students

Fabrication and Applications of In-Fiber Semiconductor and Metal Microspheres

By

Tara Sarathi

Submitted to the Department of Materials Science and Engineering on December 15, 2014, in partial fulfillment of the requirements for the degree of

Masters of Science in Materials Science and Engineering

Abstract

Currently, the synthesis of semiconducting or metal microspheres has occurred via top-down approaches, such as through ball milling or e-beam lithography, or via bottom-up approaches, such as colloidal chemistry. Top-down approaches often generate a wide particle size distribution, while bottom up approaches often involve toxic and sometimes rather expensive precursors to generate the particles. By utilizing a phenomenon known as axial thermal capillary instability, highly homogeneous semiconducting and metal microspheres are able to be generated inside of a silica fiber in a simple, inexpensive, and non-toxic top-down approach. Further applications of these in-fiber microspheres, such as the band gap shift due to localized pressure on Germanium microspheres, and terahertz plasmonic resonances on Silver microspheres, were also studied.

Thesis Supervisor: Yoel Fink

Title: Professor of Materials Science and Engineering

Professor of Electrical Engineering and Computer Science

Acknowledgements

First and foremost, I would like to thank my advisor, Dr. Yoel Fink, for being such an inspirational person and wonderful advisor not just through my graduate years, but through most of my undergraduate years as well. Without your guidance, none of the research described in this thesis would be possible. I would also like to thank Dr. Lei Wei, for helping me with the fiber fabrication in this work and for teaching me how to fabricate my own fibers. I would also like to sincerely thank Dr. Alexander Gumennik, for not only helping me with all of the break up fabrications and experiments, but for also teaching me how to be a better scientist and how to be a better person. I would also like to thank Alex Frenzel from the Gedik Group for helping me with the Terahertz Time Domain Spectroscopy measurements. Furthermore, I would like to thank the rest of the members of the lab: Michael Rein, Benjamin Grena, Chong Hou, Dr. Xiaoting Jia, and Dr. Etgar Levy for being such supportive and pleasant people to work with. I would also like to especially thank my fellow lab mate, Jefferson Clayton, for being a true friend in addition to being a brilliant colleague. And last, but certainly not least, I would like to thank my family for being so supportive of me through my graduate school years, and my taekwondo family for helping me to stay strong through my triumphs and my failures.

Table of Contents

Table of Figures

Introduction

For the past few years, recent research efforts have been aimed at generating increasingly smaller electronic and optical devices with an increased amount of flexibility and durability [1]. While several methods exist which have made advancements toward this goal, one area of research which proves promising is the integration of electronic and optical devices inside of fibers. These fiber structures allow the functional device cross section to be scaled down to the micro and nanometer scale while simultaneously allowing the device to continue lengthwise for meters. Furthermore, these fibers allow such devices to obtain a flexible, as opposed to a rigid, configuration. To date, our lab has been able to fabricate such fiber devices as surface emitting fiber lasers, thermal detector fibers, optical detector fibers, and hollow photonic band gap transmission fibers [2].

In addition, recent developments have exploited a fluidic phenomenon known as capillary instability in order to generate a top-down approach to fabricating homogenous in-fiber micro and nanoparticles [3]. Even though these particles can easily be etched out and applied to other external applications, the generation of these particles inside of a fiber opens the door to an exciting frontier of new fundamental scientific research and applications. The focus of this thesis is to explore both basic scientific curiosity and potential applications for in-fiber Germanium and Silver microspheres. This thesis is divided into four parts: Parts One and Two will describe the fabrication of Germanium and Silver fibers and their corresponding microspheres, Part Three will explore the advent of pressure inside of these Germanium spheres, and Part Four will explore the potential for terahertz plasmonic effects in Silver microspheres.

1. Fabrication of Semiconducting and Metal Fibers

1.1 Overview of Fiber Fabrication

The first step in the fiber fabrication process involves creating a structure known as a preform. This preform is multimaterial in nature, and has the same structural geometry and composition as the final fiber. The difference between the preform and the final fiber however lies in the fact that the preform has a larger cross-sectional area and is much shorter in length than the final fiber. Depending on the nature of the final fiber, the preform is often 10-30 mm in diameter, and has a length of about 30-50 cm. Figure 1 shows a variety of preforms with various structures and materials post draw.

For preforms undergoing a high temperature drawing process (greater than 2000 ^{o}C), the preform construction process begins by first assembling the drawn materials into the correct structure inside of a glass tube. Next, the glass tube is sealed at the bottom by fusing a glass rod with a similar diameter to the glass tube to the bottom of the structure via a propane/oxygen flame torch. The preform is then placed under vacuum in order to remove any trapped gas, to allow for different layers to fuse, and to allow high quality interfaces to form. Finally, the functional area (that is, the area containing the materials and structure of interest) is sealed off via the propane/oxygen torch in order to maintain the structure's integrity and to prevent any oxidation from occurring during the draw process. Figure 2 shows a finished glass preform with a Silver rod as its functional material.

(a)

(b)

Figure 1: *(a) Various post-draw preforms made with a thermoplastic cladding. Figure courtesy of Greg Hren. (b) Post-draw preform made with a glass cladding. Both preforms exhibit the bulk, beginning preform at the bottom and a scaled down portion at the top.*

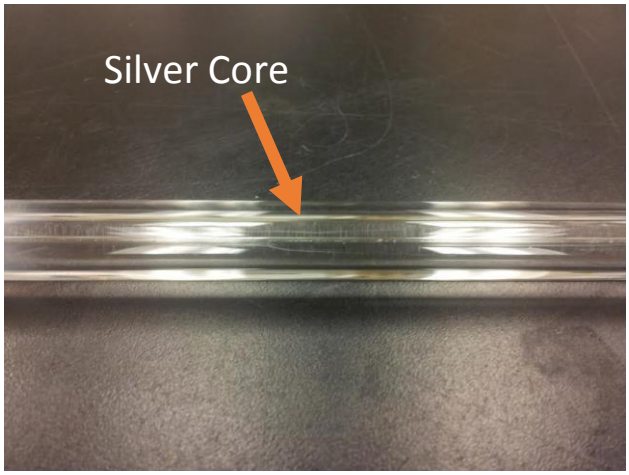

Figure 2: *A preform with Silver as the core and silica as the cladding.*

After construction, the preform is then taken to a draw tower in order to be fabricated into a fiber. Figure 3 shows both a schematic and an actual picture of the draw tower used to fabricate the necessary fibers.

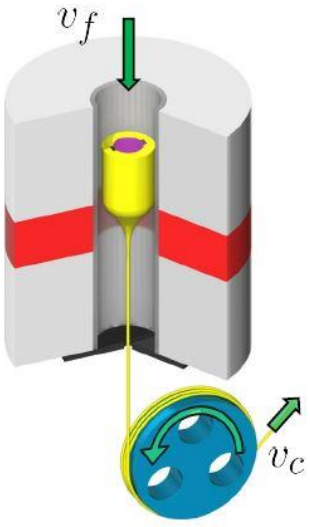

(a)

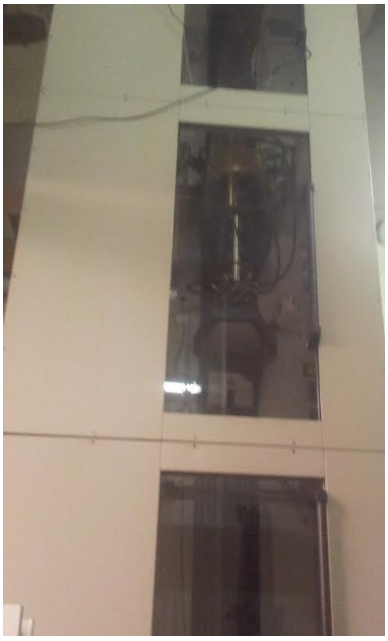

(b)

Figure 3: *a) A schematic of a fiber draw process. Figure courtesy of Guillaume Lestoquoy. b) Picture of the high temperature draw tower.*

The preform is first loaded in a preform holder at the top of the draw tower, then slowly lowered into a furnace. Once in the furnace, the preform is heated until it becomes a viscous fluid and necks down into fiber dimensions due to the force of gravity. Next, the fiber is loaded into a capstan and is continually pulled under tension. Because of the conservation of volume, the ratio of the original diameter of the preform to the resulting diameter of the fiber can be related to the speed at which the fiber is lowered into the fiber (v_f) and the speed at which the fiber is drawn by the capstan (v_c) via

$$\frac{D_{preform}}{D_{fiber}} = \sqrt{\frac{v_c}{v_f}} \qquad (1)$$

where $D_{preform}$ and D_{fiber} are the diameters of the preform and the fiber respectively. Throughout the draw, the outer diameter (OD) of the fiber is continually measured using a laser micrometer. Also, as stated earlier, throughout the draw process, both the internal and external geometry of the preform is maintained as it is drawn into a fiber. As a result, only the diameter of the cross section and the length of the preform change, and the ratio of the outer diameter to the inner diameter (ID) of the preform remain the same as it is drawn into a fiber:

$$\frac{ID}{OD} = \frac{ID'}{OD'} \qquad (2)$$

where ID and OD indicate the inner and outer diameters of the preform, and ID' and OD' indicate the inner and outer diameters of the fiber.

1.2 Drawing Process Criteria for Materials Selection

Not all materials can be drawn via this draw process. The main factor when determining if a material can be drawn is to first ensure that the materials in question can be co-drawn while both maintaining the preform geometry in a fiber and preventing any axial and cross-sectional capillary break up. In order to prevent capillary break up, viscous forces are used to oppose the interfacial energy of the capillary break up. In order to ensure this, the following criteria must be satisfied [2]:

1) At least one of the fiber materials needs to support the draw stress and yet continuously and controllably deform. With that said, at least one component should be amorphous in nature, and resist devitrification. This allows for fiber drawing to occur at reasonable speeds while still maintaining its structure. The fibers are drawn under high-stress conditions to counter surface-tension.
2) All the materials must flow (viscosity $<10^7$ poise) at a common temperature. If a crystalline material is incorporated in the preform, then it should have a melting temperature below the draw temperature.
3) The materials should exhibit good adhesion/wetting in the viscous and solid states without cracking even when subjected to rapid thermal cooling.

While in general glassy materials and polymeric thermoplastics have been used as the cladding material due to their continuous viscosity temperature dependence which in turn allows them to be drawn at high speeds, the material used in this project for the cladding is silica glass. Furthermore, this thesis will focus on using Germanium and Silver as the core materials.

1.3 Silver Fiber Fabrication

A Silver fiber was fabricated via a two-step process: first, a 1 mm diameter Silver wire, measured and cut to be 15 cm in length, was placed inside of a glass tube with a 1 mm inner diameter and a 6 mm outer diameter. The Silver wire and 1x6 mm glass tube were then placed inside of another glass tube with a 6 mm inner diameter and a 12 mm outer diameter. The placement of this structure inside of the large glass tube is done so that the fiber can be drawn to the correct diameter. This ensemble was then fused together and placed under vacuum as described previously in the preform fabrication section.

The Silver preform was then drawn using the draw tower procedure described above. A furnace temperature of 2170 ^{o}C, and v_c and v_f of 3 mm/min and 4 m/min respectively were used. By using those v_c and v_f speeds, and by using the relationship described in equation 1, the resulting outer diameter of the fiber was 1 mm, with a core size (ie the diameter of the Silver) of 83 um.

During the second step of the draw process, 20 cm of the above fabricated fiber was placed inside of a 1x6 mm glass tube. This ensemble was then placed inside of a 6x12 mm glass tube, and a preform was fabricated using the preform fabrication method described above. Figure 4 shows a schematic of this preform.

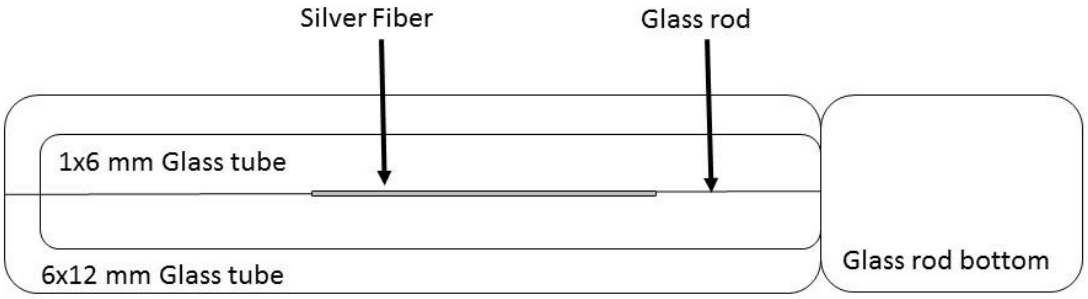

Figure 4: *Schematic of the Silver redraw preform.*

Next, the preform was then drawn using the draw tower procedure described above. A furnace temperature of 2170 ^{o}C, and a v_c and v_f of 3 mm/min and 4 m/min respectively were used. By using those v_c and v_f speeds, and by using the relationship described in equation 1, the resulting outer diameter of the fiber was 1 mm, with a resulting core size of 7 um. Figure 5 shows two SEM images of the final Silver fiber. Figure 6 shows an elemental analysis of the silver core. The results show that even after the draw, very little diffusion of the cladding material into the core has occurred.

(a)

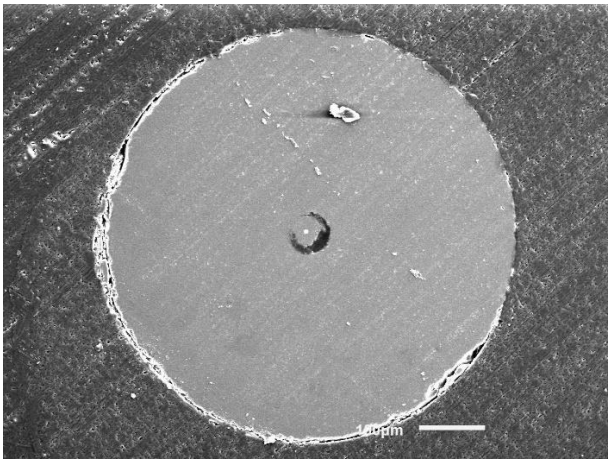

(b)

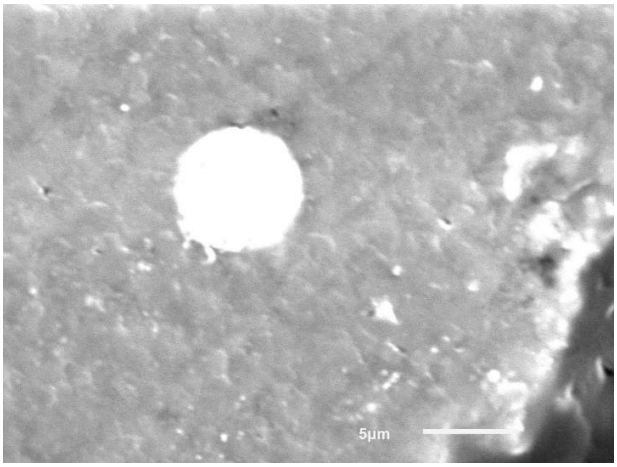

Figure 5: *(a) SEM image of the entire redrawn Silver fiber. (b) SEM image of the core of the Silver fiber.*

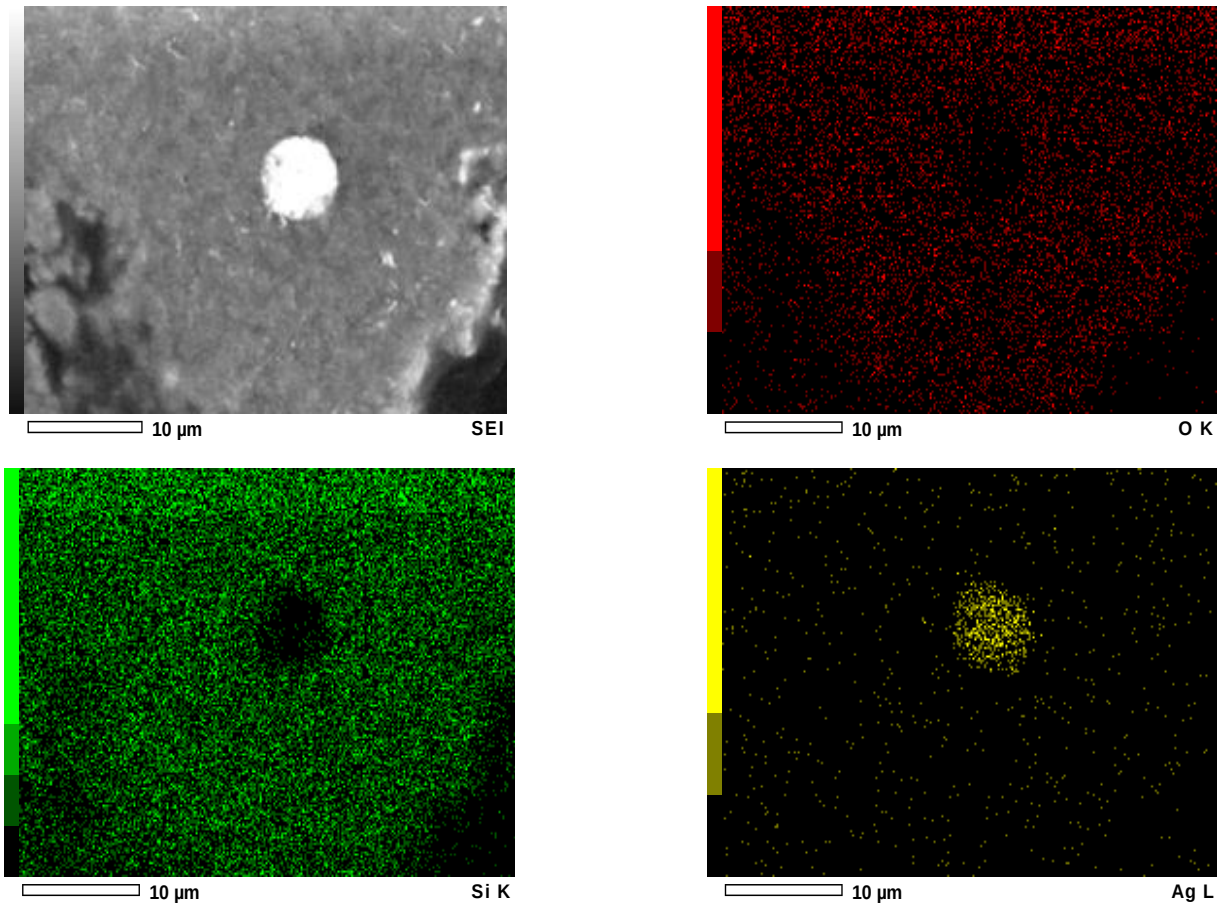

Figure 6: *Elemental analysis of the redrawn Silver fiber core. The top left picture is the original SEM image, the top right shows where oxygen is located in the structure, the bottom left image shows silicon, and the bottom right shows silver.*

1.4 Germanium Fiber Fabrication

The same procedure that was used to fabricate and draw a Silver fiber was used for fabricating and drawing a Germanium fiber. Figure 7 shows an optical microscope image for both a Germanium fiber after one draw, and a redrawn Germanium fiber. The core size after the first draw was 72 um, while the core size after the redraw was 8 um. Figure 8 shows the elemental

analysis of the Germanium fiber core after the first draw. Again, the analysis shows that diffusion is minimal between the core and cladding material.

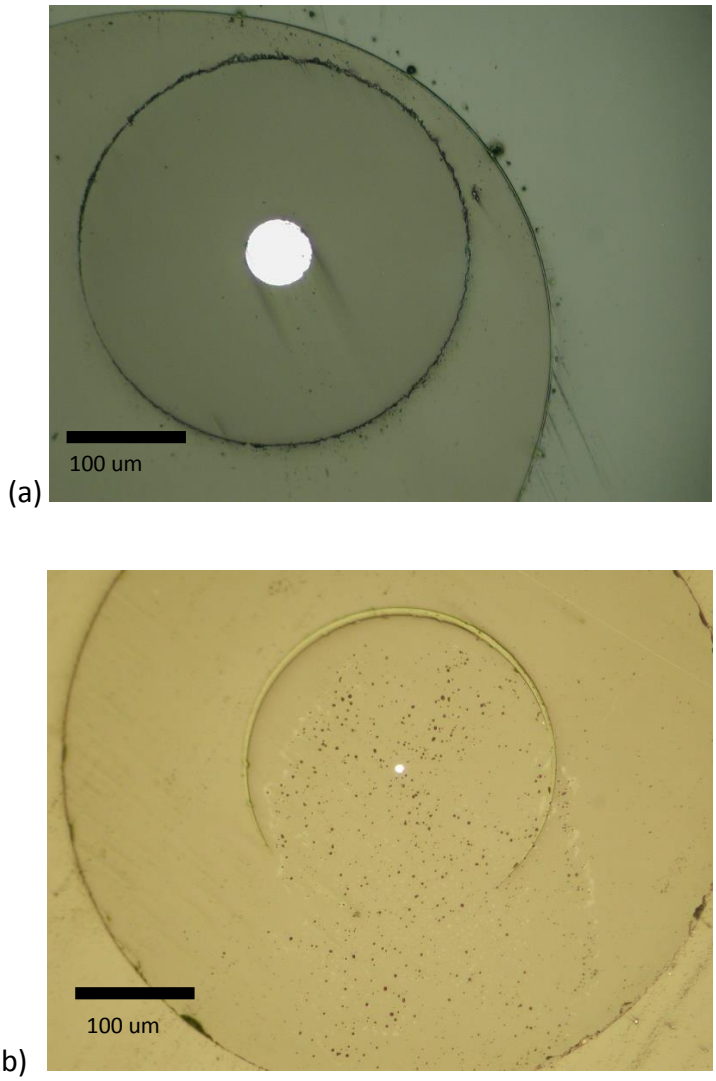

Figure 7: *(a) An optical microscope image of a Germanium fiber after one draw. (b) An optical microscope image of a Germanium fiber after a second draw.*

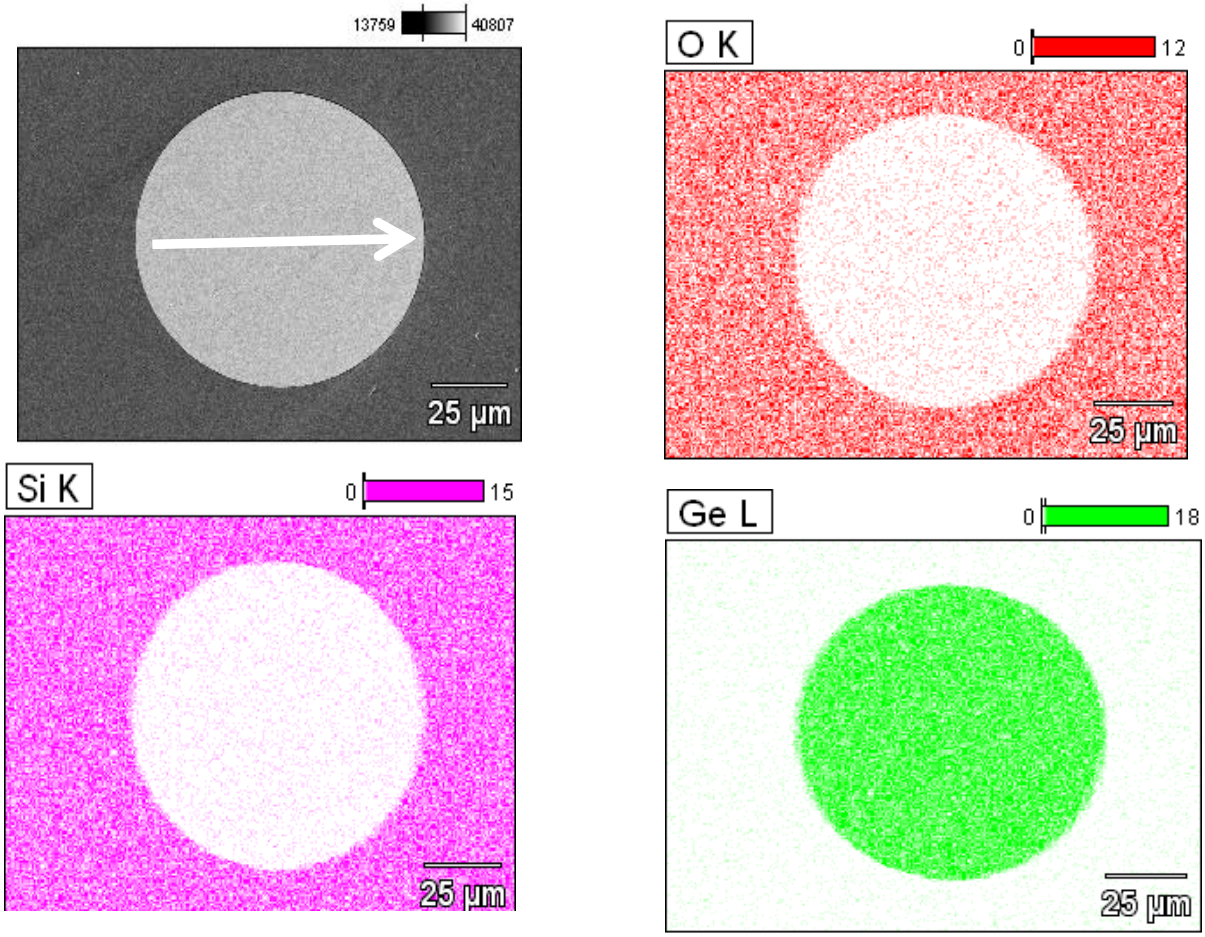

Figure 8: *An elemental analysis of the Germanium fiber after the first draw.*

2. Fabrication of In-Fiber Semiconductor and Metal Microspheres

2.1 Theory of Isothermal Capillary Instability

Even though capillary break up is an undesirable effect that needs to be prevented during the draw process, recent breakthroughs have exploited this effect in order to produce a top-down (as opposed to the 'bottom-up' approach of synthesizing particles through nucleation or self-assembly), reproducible and scalable process of generating monodisperse particles [4]. While other top-down approaches of synthesizing particles exist (eg lithography, microfluidics, etc), those processes often produce larger sized particles in low quantities [5-6]. By utilitizing this capillary break up effect, monodisperse particles of various sizes, with reported ranges from 2mm to 20 nm, can be generated in large quantities inside of fibers [4,7]. This capillary break up effect, known as the Plateau-Rayleigh capillary instability effect, works as follows. Rayleigh was the first to quantify that a cylindrical column of an incompressible, perfect fluid under capillary forces will be in a state of unstable equilibrium. In order to minimize its energy, this cylindrical column of fluid will break up into a periodic array of spheres with a wavelength of λ, provided that

$$\lambda > 2\mathrm{D} \qquad (3)$$

where D is the diameter of the cylinder [8]. In the isothermal case, a temperature gradient can be applied axially to a stationary fiber such that at the low temperature end, a highly viscous core will exist. As the temperature increases axially along the fiber, the viscosity of the core will decrease, and surface tension will start to become a significant factor. A sinusoidal modulation

will occur at the core-cladding interface, and soon the cylindrical core will locally break up into spheres. Over time, this sinusoidal modulation will spread throughout the entire core, and soon the entire core will consist of spherical particles [4]. Figure 9 shows a cartoon of this Plateau-Rayleigh instability effect [9].

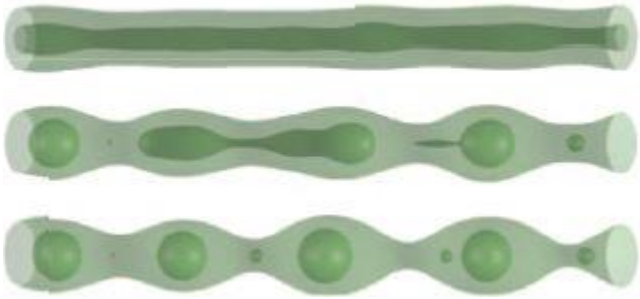

Figure 9: *A cartoon illustrating the Plateau-Rayleigh instability effect. A temperature gradient induces a sinusoidal perturbation in the system, causing the cylindrical fluid to gradually evolve into an array of spherical particles.*

The core of a fiber undergoing capillary break up by this effect can be modeled by visualizing the core as a viscous cylindrical thread inside of an infinite viscous cladding. By doing this, the break up time τ needed to produce spheres with the periodic wavelength λ is given by Tomatika's model [10]:

$$\tau = \frac{D_c \mu_p}{\gamma[(1-x^2)\Phi(x, \mu_p/\mu_g)]} \qquad (4)$$

Where D is diameter, μ_p is the viscosity of the core material, μ_g is the viscosity of the glass, γ is the surface tension between the core and the cladding materials, $x = \pi D/\lambda$, and Φ is a complex function dependent on the viscosities which is given in Tomotika's paper [10].

2.2 Theory of Axial Thermal Capillary Instability

The Tomotika model and method of capillary break up, however, is only valid for an isothermal case in which a constant temperature is held at one end of the fiber. This method is very useful for a low temperature break up of polymers and chalcogenide glasses where the viscosities between the core and cladding are similar. This method is not as practical for high viscosity contrast materials systems, which is the case for Silver or Germanium and glass. In the latter case, the fastest growing λ would be quite large, and thus large particles would be produced after a large amount of time. As a result, much more recently a break up process has been developed for these systems which has the ability to produce submicron sized particles by utilizing an axial thermal gradient and a moving fiber [3]. During this process, a fiber is continuously fed into a spatially localized flame, causing local melting of the core material to occur in a fixed location in space. Capillary instability due to the surface tension between the molten core and the soften glass cladding then causes a sphere to form at the tip of the cylindrical core in order to minimize its surface energy. As this fiber leaves the flame, the sphere then cools and solidifies, effectively becoming 'frozen' inside of the glass cladding. This process of continuously feeding the fiber into a flame to create spheres can be thought of as

analogous to the way the flow rate of water in a faucet can influence droplet formation. Figure 10 shows both a cartoon and an image of this break up process for a fiber with a silicon core [3].

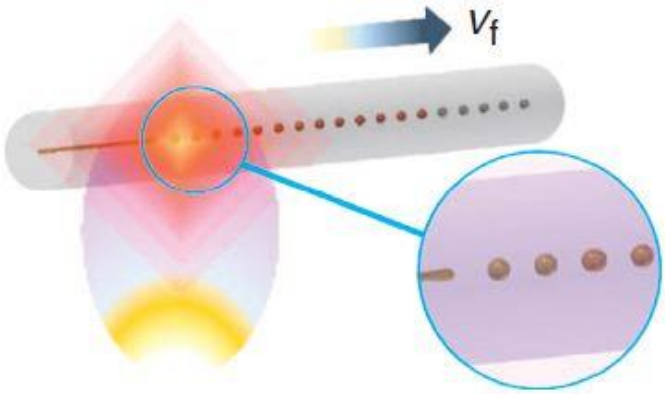

(a)

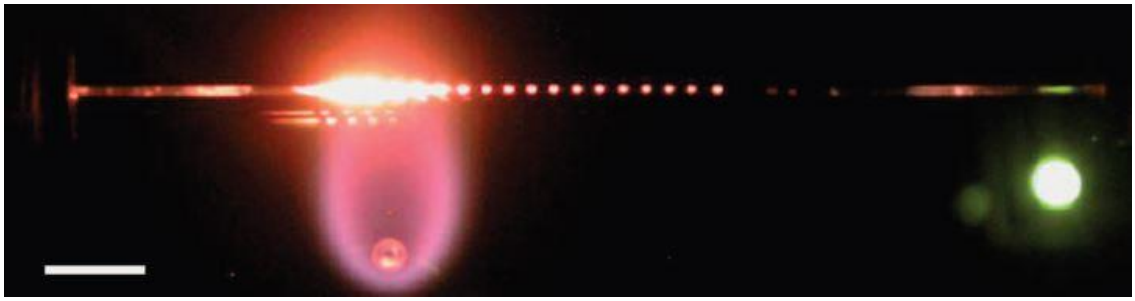

(b)

Figure 10: *(a) A cartoon of the thermal gradient break up process. A fiber is continuously feed into a flame, and due to capillary instability, sphere formation occurs at the tip of the cylindrical core. As the temperature decreases, these spheres solidify and become 'frozen in the cladding. (b) An image of a silicon core fiber embedded in a silica cladding undergoing this thermal gradient break up process.*

As mentioned earlier, if the isothermal Tomatika model were followed, the break up period λ, is dependent on the ratio of $\mu_{core}/\mu_{cladding}$, as discussed in equation 4. As an example, Figure 11 shows the temperature dependence of the viscosity of Silver and silica respectively [3,11]. Since

break up can only in theory occur in the temperature range of between the melting and boiling point of the core material, which for the case of Silver in silica, in the temperature range of 960-2160 ^{o}C [12], this ratio is on the order of 10^{8}-10^{12}. This results in $\lambda >> \pi D$ and thus results in the formation of large sized particles. However, recent studies have been able to use this method to generate submicron sized particles, indicating that the classical Tomatika model is not enough to describe this phenomenon [3].

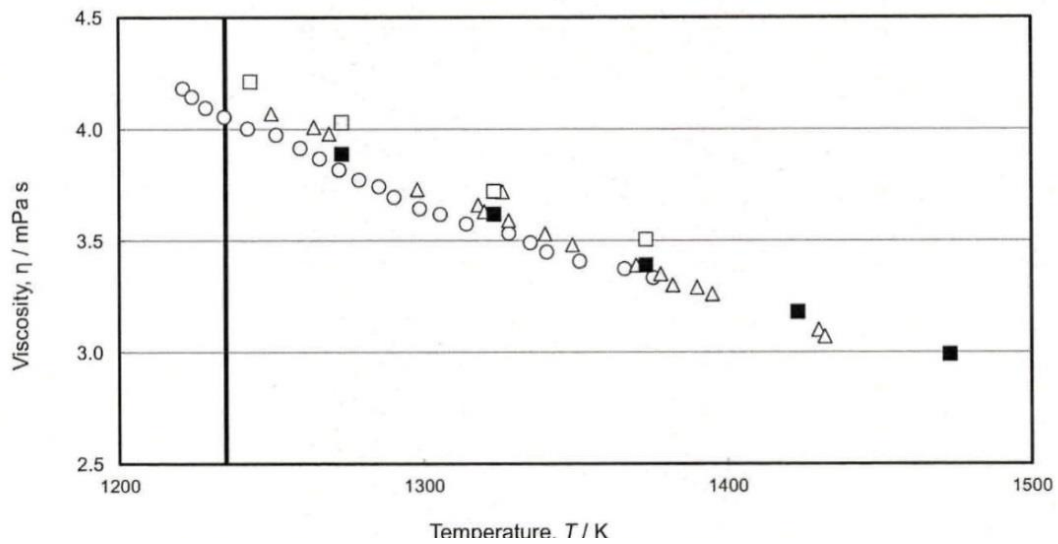

(a)

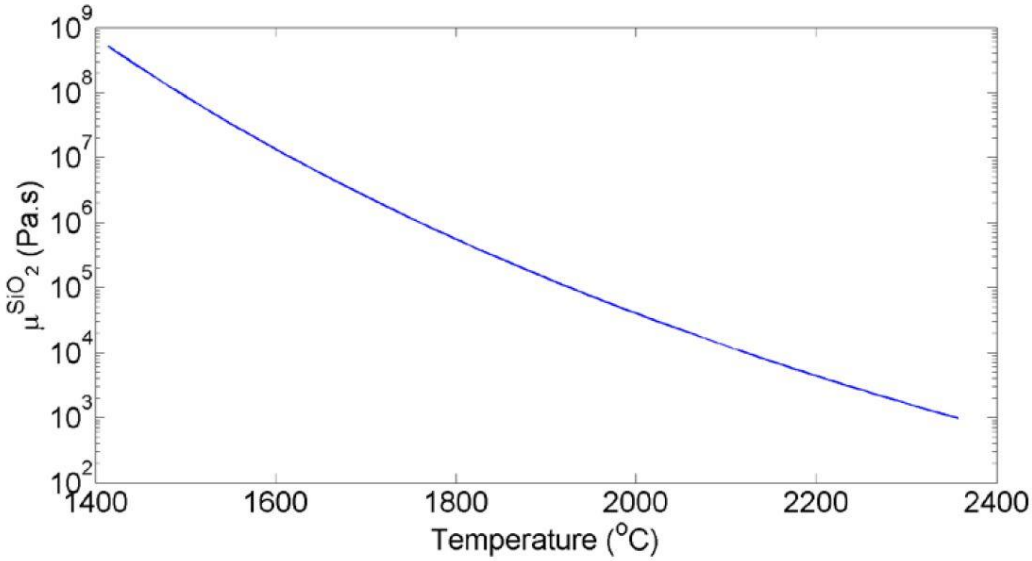

(b)

Figure 11: *(a) Graph depicting the temperature dependence of the viscosity of Silver. In the temperature range of interest, the viscosity of Silver only various by approximately 20%. (b) Graph depicting the temperature dependence of the viscosity of silica. The viscosity of silica various much more drastically over the temperature range of interest than Silver. This change suggests that in the classical Tomotika model, the resulting size of the particles will be larger than submicron sized. This also suggests that temperature dictates the resulting size of the particles.*

Even though a modified Tomatika model can be used to explain this break up phenomena, a simpler and alternative viewpoint can be considered which yields an accurate prediction of the resulting particle diameter as a function of the speed at which the fiber moves through the flame, or the feed speed v_f [3]. As mentioned previously, an intuitive analogy to this phenomenon is the formation of a drop of water from a leaky faucet. As the fiber is fed into the flame at v_f, the interfacial tension between the core and the cladding, γ_p, causes the molten core to be pinched off at a fixed pinch off location in space, x_p. The velocity at which core pinching occurs is

$$\mu_p \cong \frac{\gamma_p}{\mu_{cladding}} \qquad (5)$$

By knowing this, and by knowing that the wavelength λ can also be interpreted as the amount of fiber entering the flame during the time $\frac{D}{2\mu_p}$, the break up wavelength, and thus the size of the resulting particles, can be related to the feed speed by

$$\lambda \cong v_f \frac{D\,\mu_{cladding}}{2\gamma_p} \qquad (6)$$

Even though Equation 6 suggests a linear correlation between the break up wavelength and the feed speed, this is not quite the case. As the feed speed increases, the pinch off point occurs deeper within the flame, which in turn causes faster pinching speeds since the temperature is higher deeper in the flame. In addition, the viscosity of the cladding, especially of silica, is highly temperature dependent. Figure 12 shows an illustration of this pinch off analysis [3].

In summary, the key points from this analysis is that as opposed to isothermal capillary break up, where the break up wavelength is only independently controlled by varying the temperature, the thermal gradient capillary break up process utilizes both the fiber feed speed and flame temperature to control the size of the resulting particles. These two 'tuning knobs' can then be used to create particles in the submicron regime, which is not possible to achieve with the isothermal break up process for materials that have a large viscosity contrast ratio.

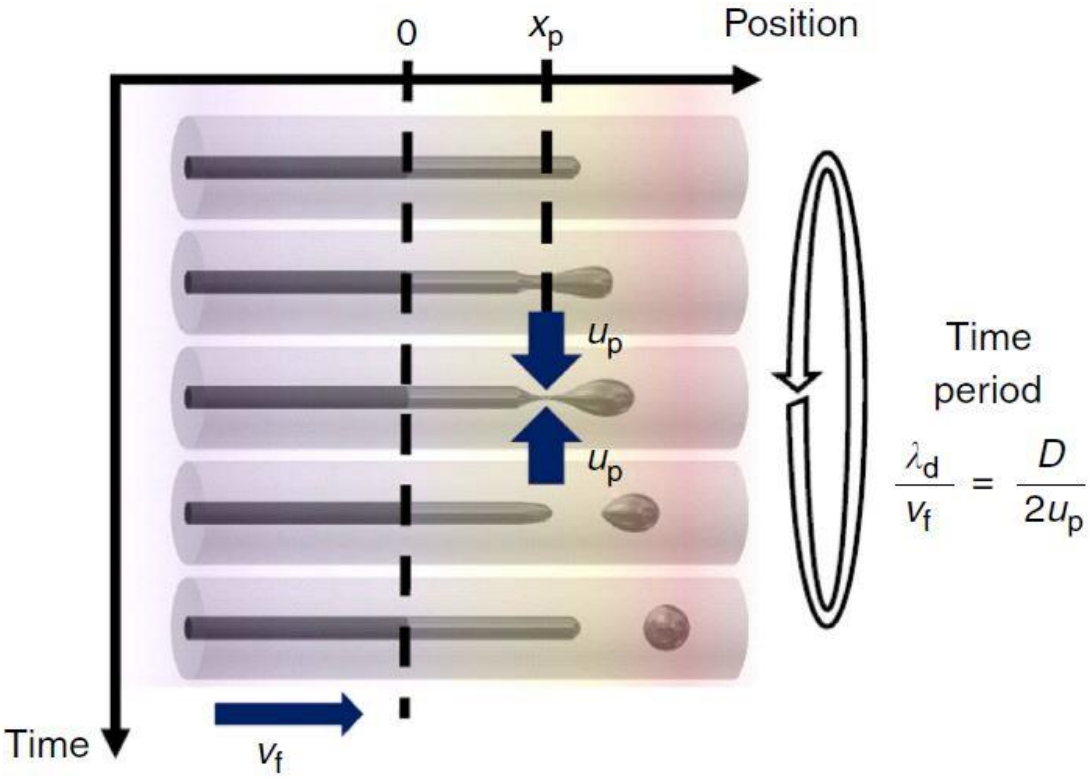

Figure 12: *An illustration depicting the pinch off mechanism and point in space. Based off of dimensional analysis, the wavelength of the break up can be related to the feed speed.*

2.3 Building the Thermal Axial Capillary Instability Break Up Instrument

Figure 13 shows the capillary break up setup that was designed and built for the purposes of tapering (ie scaling the size of a fiber down) and breaking up glass/semiconducting or metal fibers. The set up works as follows. First, a fiber is loaded into the set up by threading it through both motors and fiber holders. The function of the fiber holders is hold the fiber in place and to only expose a small section of the fiber to the heat source. Next, the fiber is pulled such that it is under tension. After loading the fiber into the instrument, a hydrogen and oxygen flame torch is ignited, and the flow rates of the two gases are adjusted in order to achieve the desired break up temperature. Finally, the motors pull the fiber from left to right, and over time the entire core of the fiber is broken up into spheres. Figure 14 shows a top view of the instrument, and in this top view a fiber being exposed to the hydrogen oxygen flame can be seen.

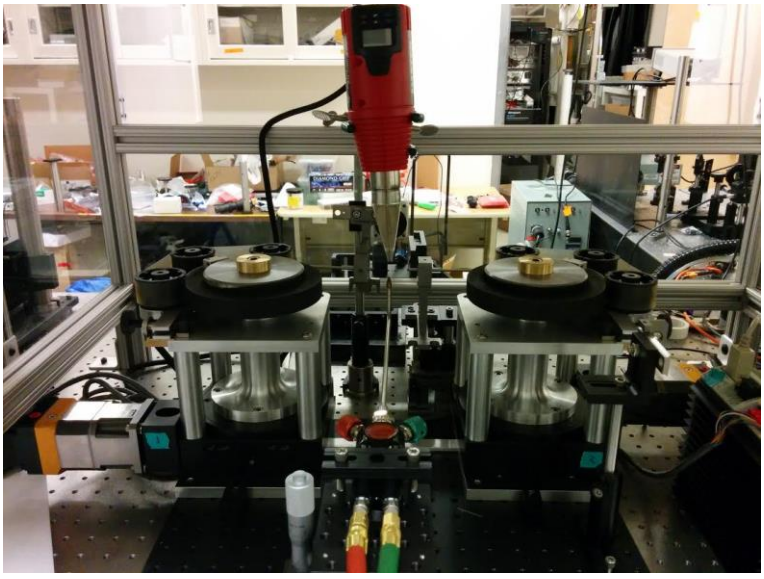

Figure 13: *A picture of the capillary break up set up. Two capstans are responsible for rotating a fiber through a hydrogen oxygen flame torch. A heat gun has been installed overhead to allow for the break up of lower temperature polymeric fibers.*

(a)

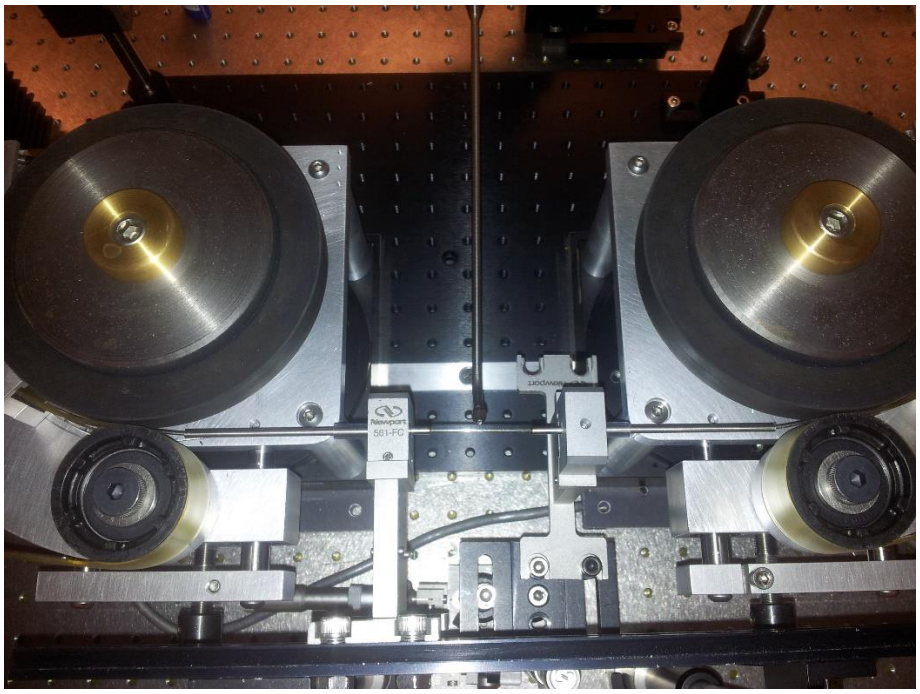

(b)

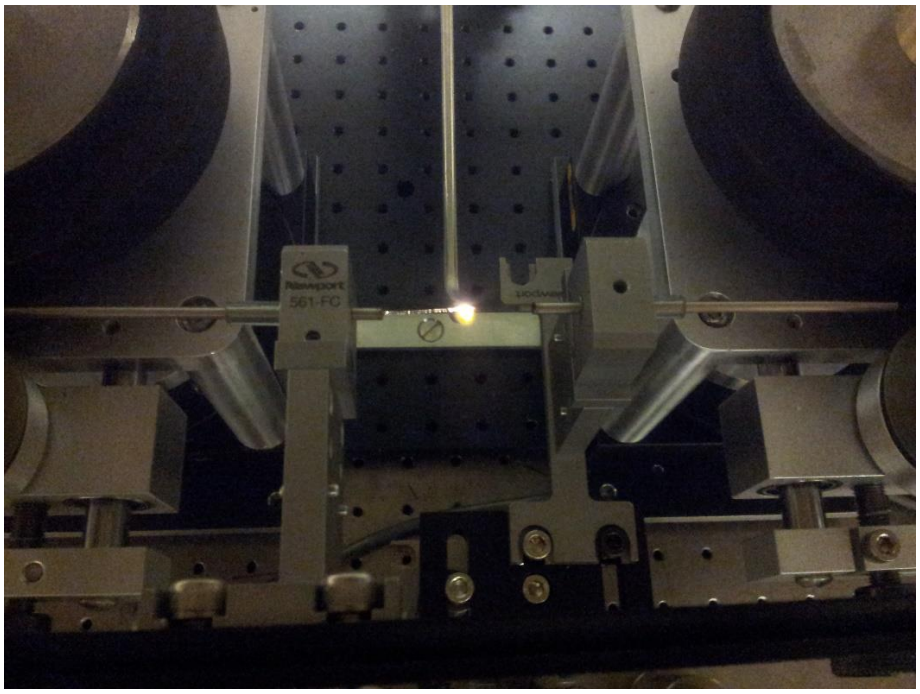

Figure 14: *(a) A top view picture of the break up set up. A fiber has been threaded through both capstans and fiber holders. (b) The same fiber is exposed to a hydrogen oxygen flame torch.*

When designing and building this set up, several factors needed to be taken into consideration. First, the set up needed to be able to produce the high temperatures necessary for capillary break up to occur. In order to achieve this, a hydrogen and oxygen flame torch was installed in the set up. During the experiment, the temperature can be adjusted by adjusting the flow rates of hydrogen and oxygen. These flow rates are measured in units of L/min. While higher flow rates of both hydrogen and oxygen correspond to a hotter flame, in general increasing the flow rate of oxygen while keeping the hydrogen flow rate constant will have the larger temperature increase effect. While the hydrogen and oxygen flame torch generates the correct temperature range for breaking up semiconducting and metal cored fibers, the temperature range is too hot if the instrument is to become versatile enough to handle the low temperature break up of polymeric fibers. In order to accommodate a lower temperature range, a heat gun was added to the instrument, as can be seen in figure 13.

The second consideration taken into account is that the fiber needed to be able to horizontally move through the flame at both a desired speed and high stress. In order to achieve the desired speed, two step motors were attached to custom built, rotating capstans. These components can be seen in figure 13. The step motors can provide rotational velocities from 0.001 to 1000 rotations/s. This translates to a linear velocity range for the fiber of 0.025 to 25000 um/s. To ensure that the fiber is under enough stress during the break up process, the fiber must be pulled while being loaded into the instrument. In order to maintain this stress during the break up process, both motors must both initiate and be pulling at the same time. An extensive Labview program which independently controls both motors was written in order to satisfy this condition. This independent but simultaneous control of the motor can allow unique

experiments on fibers to be conducted. For example, by having one motor rotate faster than the other, a fiber can be tapered down to a smaller size before undergoing the break up process. In addition, the motors can also be programmed such that after a length of time, both motors can change speeds and maintain that speed for a set length of time before changing to another speed. This can allow for different sphere sizes to be formed inside the fiber in a periodic fashion.

Third, since the fiber cladding is made out of glass, the fiber must not break as it rotates through the instrument. To prevent this, the capstans, which are in contact with the glass fiber and rotate the fiber through the instrument, are made out of rubber, and a silicone band was used to help hold the fiber gently against the capstans. Both of these materials have proved to be gentle materials on the fiber and both help to guide the fiber safely through the set up. Figure 15 shows how the fiber is gently held against the capstan.

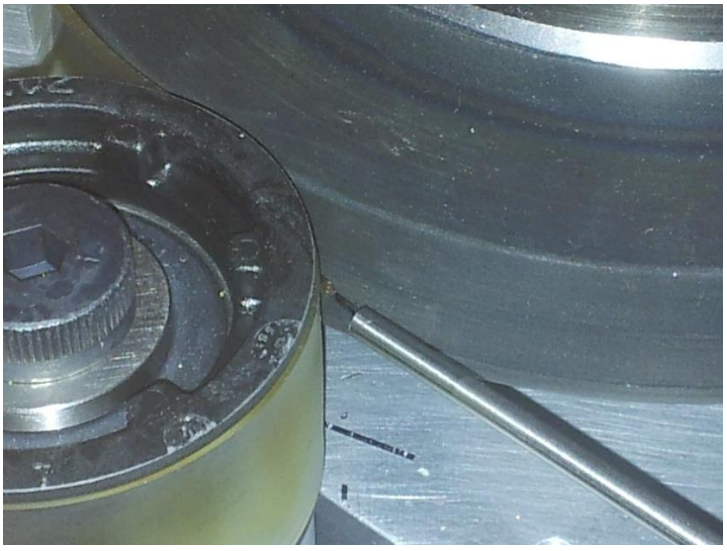

Figure 15: *A picture showing how a fiber is held against the black capstan by a silicone conveyor band*.

Finally, and most importantly, the fiber must be aligned in a perfectly straight fashion between both capstans before undergoing the break up process. If this condition is not met, then one of two possible mishaps can occur. First, if one end of the fiber were placed slightly higher in the set up than the other, then an extra component of stress would be added to the fiber, which would eventually cause the fiber to break as it rotated through the instrument. Second, when the fiber is initially introduced to the flame, if there is any misalignment, then the fiber would heat up nonuniformly. This would cause one end to heat up faster than the other, and as a result one end would soften faster than the other and droop. This would then cause a kink to occur in the fiber. As the fiber moves through the small diameter of the fiber tube holders, the kink would brush up against the fiber tube holder and cause another kink with a larger amplitude to occur in the fiber. The resulting fiber, if it does not break, would be filled with kinks instead of a perfectly straight fiber with uniform sized spheres. To ensure the alignment of the fiber before it undergoes capillary break up, one fiber holder was installed on a stage translator, which allows for the fiber to be finely adjusted after being loaded into the set up. In addition, and camera with up to 14x magnification was installed, which can provide better insight into how aligned the fiber is in the set up.

2.4 Capillary Break Up of Germanium Fibers

For the capillary break up of Germanium spheres, the fiber described in the 'Germanium Fiber Fabrication' section was used. This fiber, which contains a 70 um core size with a 1 mm outer diameter, was feed through the set up with a linear velocity of 75 um/s. The hydrogen and oxygen flow rates were 0.33 L/s and 0.12 L/s respectively. Figures 16 shows an optical microscope image of the fiber after undergoing capillary break up. The resulting spheres were homogenous in size with a diameter of 70 um.

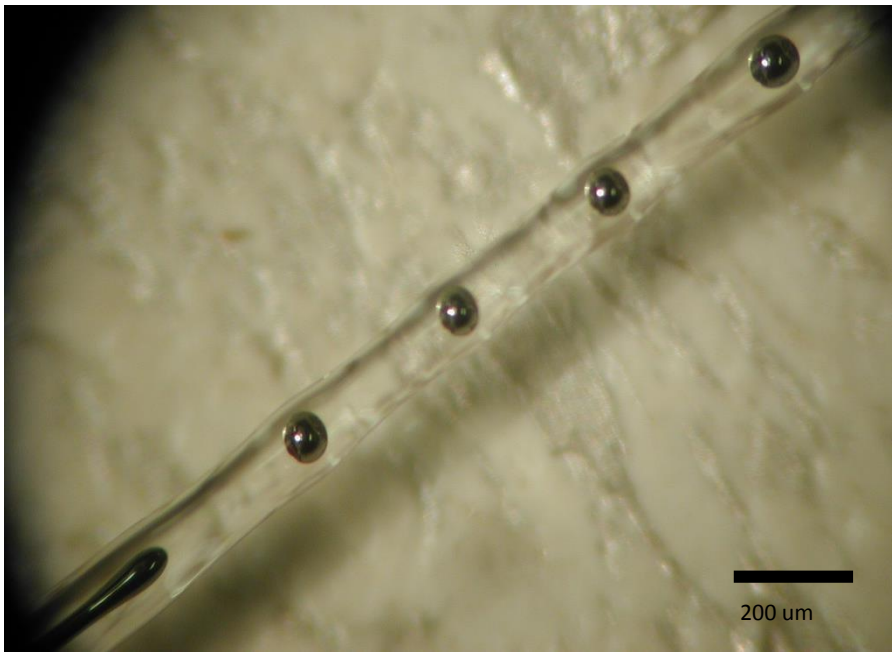

Figure 16: *An optical microscope image of in-fiber Germanium spheres.*

These Germanium spheres were also etched out of the glass and taken to an SEM to image. The resulting SEM image can be seen in Figure 17. For these large spheres, after being removed from their glass encasing, they broke in half. This is most likely due to the large amount of stress that are generated around these spheres after solidification. More on this topic will be discussed in the following section. On the other hand, when spheres which were generated from the smaller, redrawn Germanium fiber were etched and imaged with the SEM, those spheres did not break, as can be seen in Figure 18. Since these spheres are smaller, a smaller amount of stress is built up on them after solidification. As a result, cracks are seen to be nucleating on the surface of the spheres, but the stress is not enough to cause the spheres to break in half.

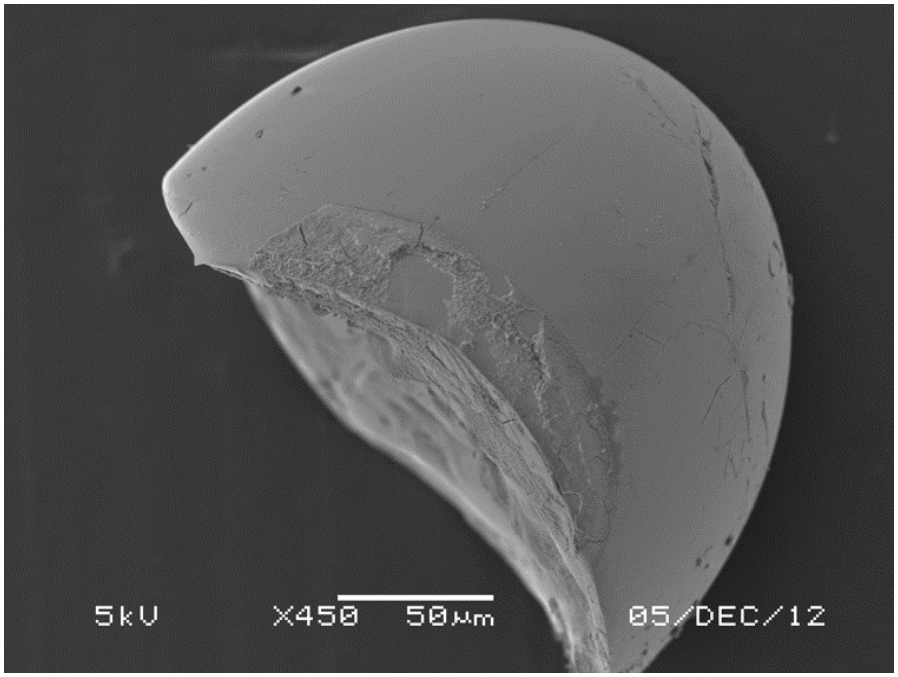

Figure 17: *An SEM image of a Germanium sphere made from a 70 um core Germanium fiber.*

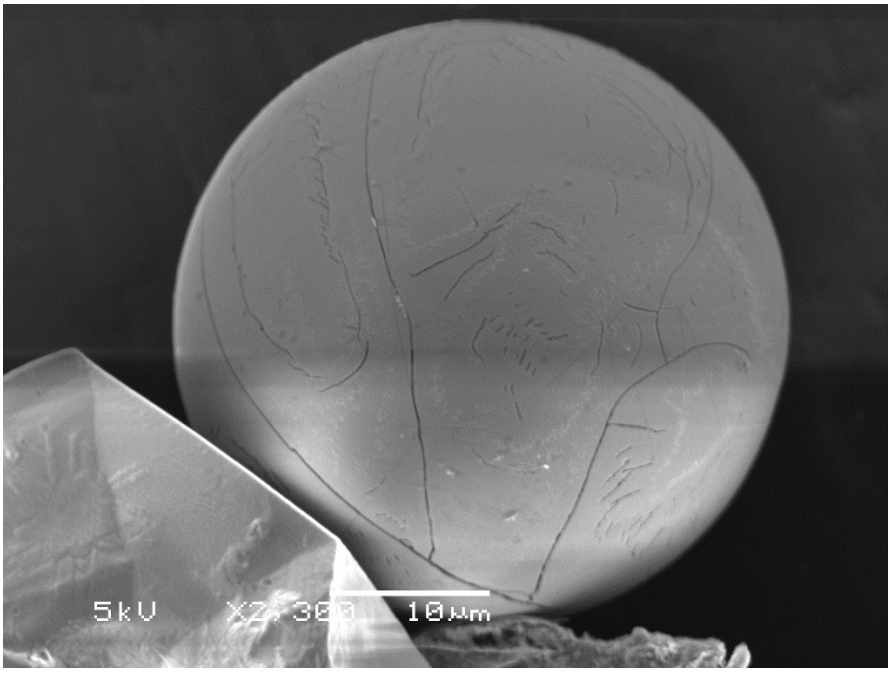

Figure 18: *An SEM image of a Germanium sphere made from a 7 um Germanium fiber.*

2.5 Capillary Break Up of Silver Fibers

The redrawn Silver fiber described in the 'Silver Fiber Fabrication' section was used for the following capillary break up experiment. The redrawn Silver fiber, with a core size of 7 um and an outer diameter of 1 mm, was fed through the break up set up at a linear velocity of 75 um/s. The hydrogen and oxygen flow rates were 0.26 and 0.06 L/s respectively. An image of the resulting spheres can be seen in Figure 19. The final diameter of the Silver spheres is 30 um.

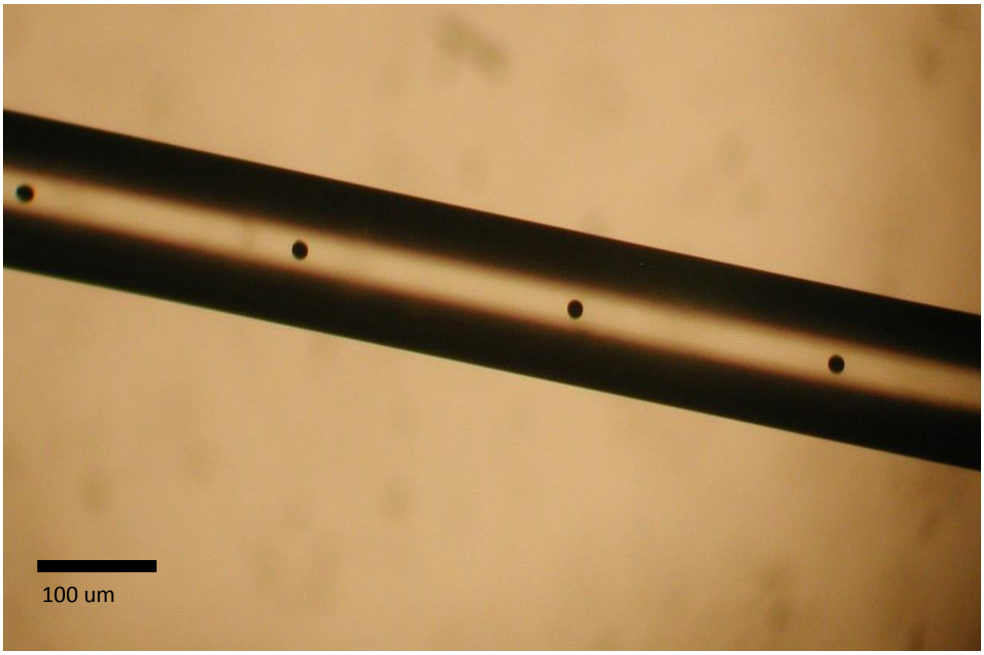

Figure 19: *An optical microscope image of in-fiber Silver spheres.*

3. Pressurized Semiconducting Spheres

3.1 Theory of Stressed Semiconducting Spheres

During the break up process, as the Germanium core solidifies into its new spherical geometry, the spherical particle will expand. Since the particle is not expanding in free space, but instead inside of a semi-rigid silica wall, the particle will exhibit some stress. Figure 20 illustrates this solidification and resulting stress principle. Because this particle is undergoing uniform solidification, its radial and tangential stress components can be taken to be equal in magnitude, and both of those components can be taken to be equal to the hydrostatic pressure P. The case of a spherical inclusion expanding in a semi-rigid vessel has been studied, and its hydrostatic pressure can be given by [13]:

$$\sigma_{rr}^{S}(r) = \sigma_{\theta\theta}^{S}(r) = \sigma_{\varphi\varphi}^{S}(r) = -\frac{4\,K_S G_M}{3K_S+4G_M}\alpha = -P \qquad (7)$$

where K_s is the bulk modulus of the Germanium sphere, G_m is the shear modulus of silica, and α is the nominal volume expansion upon solidification, which is given by:

$$\alpha = \frac{V_{\text{solid}}}{V_{\text{liquid}}} - 1 = \frac{\rho_{\text{liquid}}}{\rho_{\text{solid}}} - 1 \quad (8)$$

where ρ_{solid} and ρ_{liquid} are the free-space densities of the sphere material as solid and as liquid respectively [13]. When all of these materials values are inserted into the equation [14-16], it is predicted that the Germanium spheres are experiencing a volume pressure (ie a pressure inside of the sphere as opposed to the surface) of about 1.5 GPa.

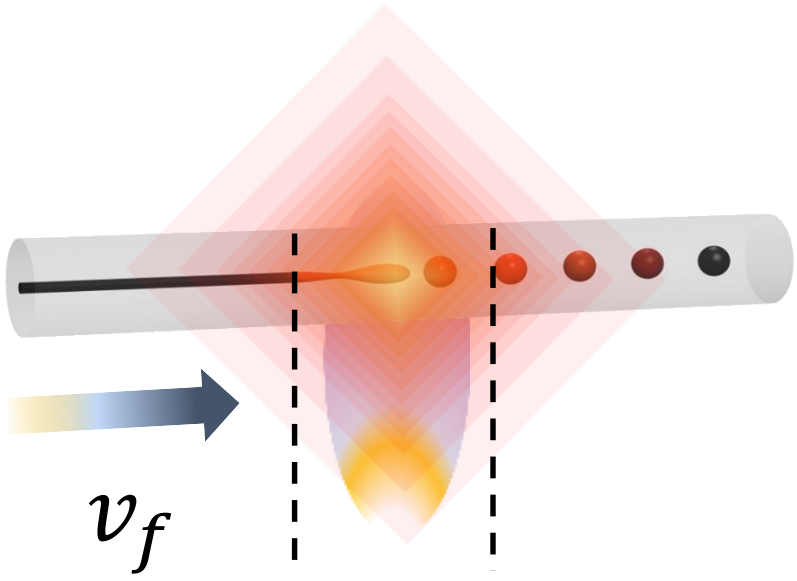

(a)

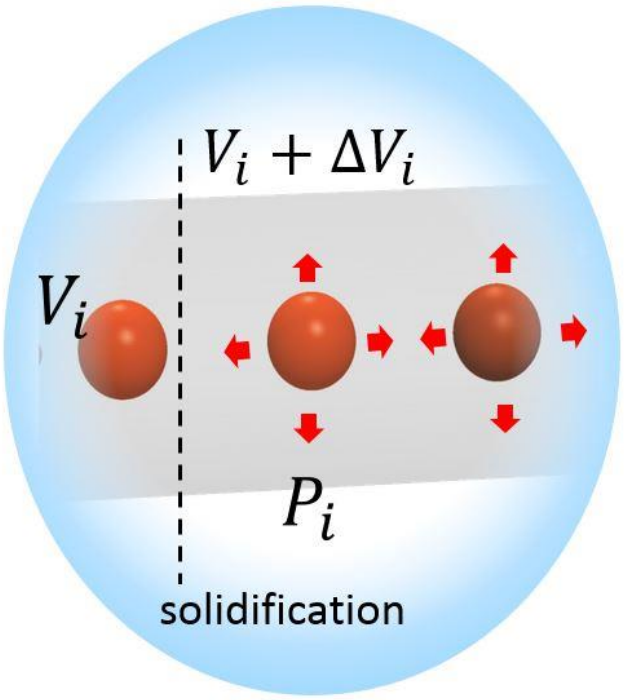

(b)

Figure 20: *(a) A cartoon illustration the melting and solidification process of a sphere undergoing axial thermal capillary break up, and (b) a cartoon illustrating how upon solidification, the sphere expands against its semi-rigid silica surrounding. Courtesy of Alexander Gumennik.*

3.2 Band Gap Shift in Germanium Spheres

One method of verifying if these pressurized Germanium spheres are experiencing 1.5 GPa of stress is by measuring a shift in the band gap. Figure 21 shows the band structure for Germanium [17]. Applying a stress to a material changes the bond lengths and thus the crystal structure of a material. Since a band structure depends on the crystal structure of a material, it makes sense that an additional stress will alter the band structure and thus the position of the band gaps.

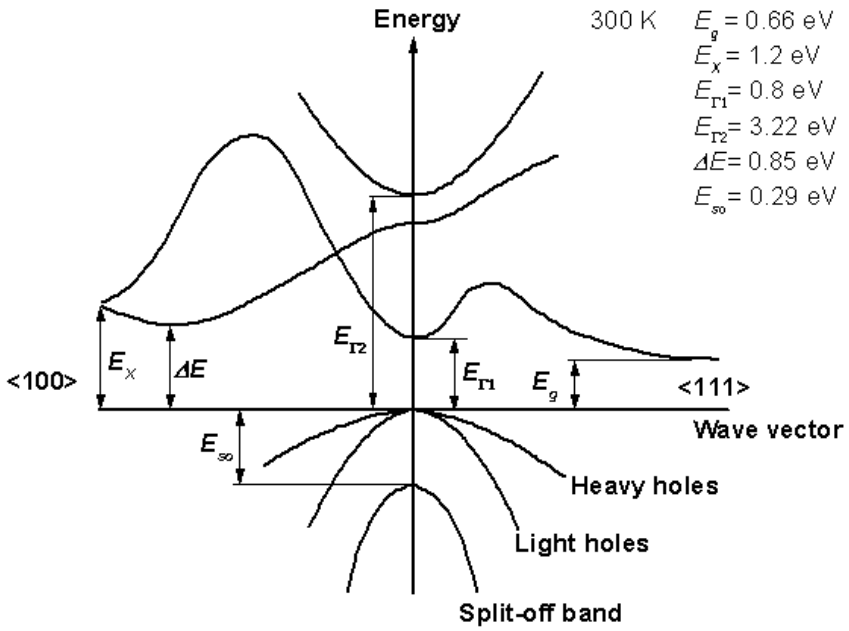

Figure 21: *The unperturbed band structure of Germanium.*

The two band gaps that were examined in this experiment were the lowest (indirect) band gap, located at E_g = 0.66 eV, and the lowest energy direct band gap, located at E_r = 0.8 eV. For these two band gaps, the change in the band gap energy with respect to pressure is given by [18-19]:

$$\frac{dE_g}{dP} = 0.050\ \frac{eV}{GPa}; \quad \frac{d\Gamma_I}{dP} = 0.121\ \frac{eV}{GPa} \qquad (9)$$

In order to measure the band gap shift, FTIR measurements were taken on a Germanium fiber sample. This sample contained both a section with the original, redrawn Germanium core (core size: 7 um), and Germanium spheres that were formed by allowing the redrawn Germanium fiber to undergo the capillary break up mechanism (sphere size: 30 um). Figure 22 shows the sections of the fiber that were examined under the FTIR and their corresponding results. Figure 23 shows the average of several measurements taken in both the Germanium core and spheres, and clearly shows the band gap shift in the spheres. The indirect band gap shifted to a higher energy by 0.06 eV, while the direct band gap shifted to a higher energy by 0.09 eV. When these shifts are inserted into Equation 9, the resulting pressure is found to be 1.8 GPa. This result is about the same as the theoretical pressure. Currently, other members of our lab are studying how to utilize this pressure in various applications.

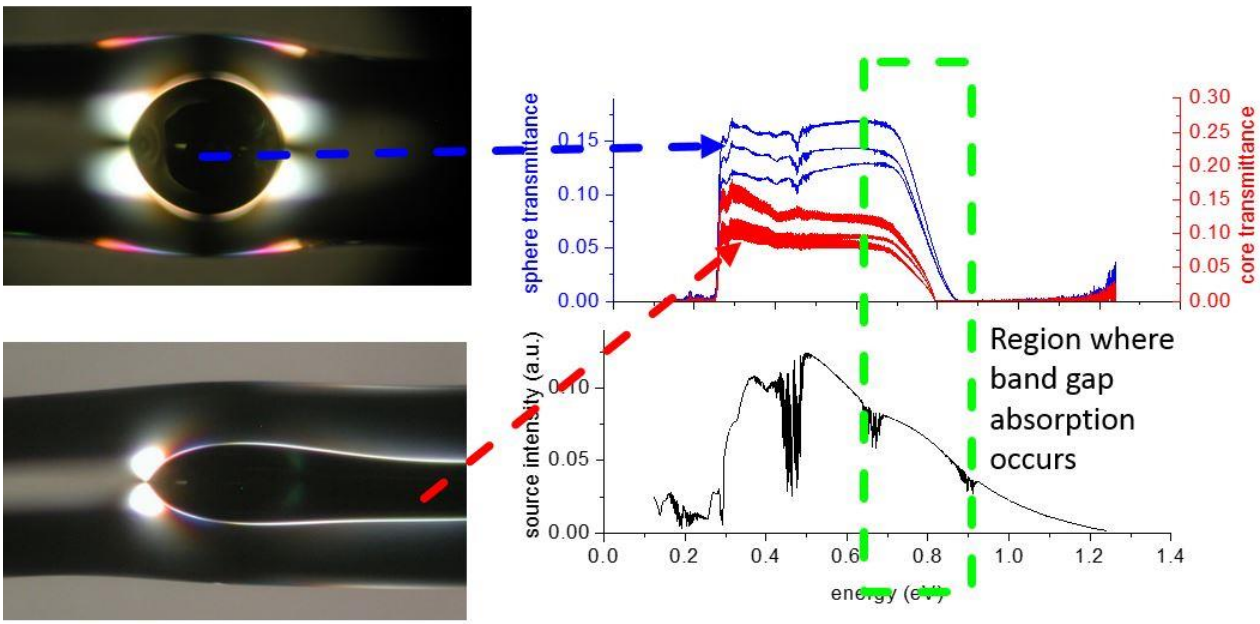

Figure 22: *FTIR measurements taken from a Germanium sphere and a Germanium core. The red curves correspond to the measurements taken from the core, while the blue curve corresponds to measurements taken from the spheres. These three measurements were then averaged, and the resulting curve was zoomed in to the region designated by the green box. These results are shown in Figure 23. Figure courtesy of Alexander Gumennik.*

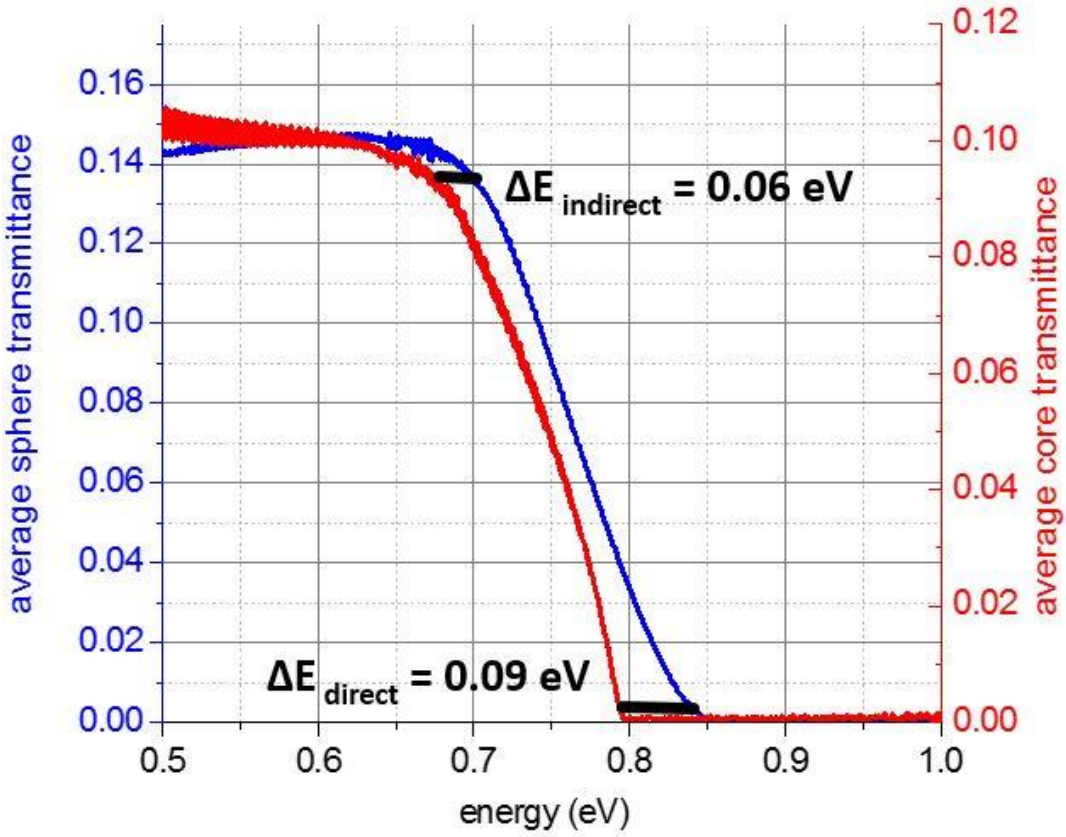

Figure 23: *The averaged FTIR curves for the spheres (blue) and core (red). The indirect band gap shifted by an energy of 0.06 eV between the core and the spheres, while the direct band gap shifted by an energy of 0.09 eV between the core and the spheres. Figure courtesy of Alexander Gumennik.*

4. Plasmonic Effects in In-Fiber Metal Spheres

4.1 Theory of Surface Plasmon Resonances

Up until the last few decades, the terahertz regime of the electromagnetic spectrum (100 GHz-30 Thz) was known as the 'terahertz gap' due to a lack of ability to generate and detect radiation in that range [20]. As the technology to generate and detect this range of radiation began to develop, research efforts have been focused on being able to produce a scalable, low cost, and time efficient way of generating terahertz radiation. Once this is accomplished, breakthroughs in several real world applications can occur: terahertz imaging of materials could greatly impact pharmaceutical, semiconductor, and polymer quality control, medical imaging with terahertz radiation can provide a safe, noninvasive way of imaging, for example, cancer cells, chemical sensing in the terahertz regime can provide a higher degree of chemical selectivity due to many chemicals containing a unique 'fingerprint' in that regime, and the ability of terahertz radiation to penetrate through opaque materials can be of great use for security applications [21]. One way that terahertz radiation can be generated in a low cost, scalable way is through surface plasmon resonances (SPRs) in the terahertz regime [22].

In general, surface plasmons are a quanta of surface charge density oscillations. For metals, surface plasmons can conceptually be thought of in the following way. First, one of the fundamental properties of metals is that their outer shell electrons are loosely bound to each individual atom. This in turn effectively creates a 'sea' of conduction electrons that can freely move around within the bulk of the material. This sea of electrons is often referred to as a 'free

electron gas', and is modeled as such in order to obtain various optical properties of metals [23].

Since electrons carry a charge, electromagnetic waves can drive the free electrons in a metal to oscillate. Much like with an oscillatory model, such as pushing a child on a swing, there exists a certain resonance frequency which can cause a free electron to respond more readily to the electromagnetic driving force than other frequencies. This resonance frequency elicits interesting optical properties, such as a unique absorption peak and a frequency dependent dielectric constant for the metal. The classic model which is used to describe this free electron gas' interaction with a driving electromagnetic field is known as the Drude-Sommerfield model. The starting equation for this model is similar in form to most oscillatory models [23]:

$$m_{\mathrm{e}}\frac{\partial^2 \mathbf{r}}{\partial t^2} + m_{\mathrm{e}}\Gamma\frac{\partial \mathbf{r}}{\partial t} = e\mathbf{E}_0 e^{-i\omega t} \qquad (10)$$

with the first force term consisting of the electron's effective mass (m_e) and the electron's acceleration from its initial position, the second damping term consisting of a damping coefficient r and the particle's velocity, and the third driving force term consisting of the driving electric field's amplitude $\mathbf{E_o}$ and frequency ω. Note, in this case, there is no third restoring force term on the left hand side of the equation because these are considered free electrons, not bound. Brongersma gives a detailed solution to this equation, but when this equation is solved a frequency dependent dielectric constant appears [23]:

$$\varepsilon_{\mathrm{Drude}}(\omega) = 1 - \frac{\omega_{\mathrm{p}}^2}{\omega^2 + \Gamma^2} + i\frac{\Gamma\omega_{\mathrm{p}}^2}{\omega(\omega^2 + \Gamma^2)} \qquad (11)$$

where ω_p is the volume plasma frequency, given by [23]

$$\omega_{\mathrm{p}} = \sqrt{ne^2/(m_{\mathrm{e}}\varepsilon_0)} \qquad (12)$$

For metals, such as Silver and Gold, the real part of the dielectric constant ϵ is negative, which is a crucial property needed when considering surface plasmon resonances. In addition, while this model does describe the dielectric constant well for longer wavelengths, an additional restoring term needs to be taken into account in this model to accurately describe the intraband transitions that occur in metals at short wavelengths (usually within the UV region). However, since this thesis is mainly concerned with the long wavelength end of the electromagnetic spectrum, the corrected Drude-Somerfield model will not be discussed.

Even though the above discussion specifically talked about how an electric field can cause a single electron in an electron gas to oscillate and thus give rise to a dielectric constant, electromagnetic waves can cause collective oscillations of the electron density at the surface of a metal. These collective oscillations can then naturally couple to electromagnetic waves, which is why these collective oscillations are sometimes referred to as 'surface plasmons polaritons'. [23]. Since these collective oscillations occur at the surface of a metal, in order to model these surface plasmons it is necessary for there to be two mediums and an interface separating the two mediums. For the purposes of our in-fiber particle system, the simplest way to examine and model the existence of surface plasmons is to first look at a plane geometry. The reasoning behind this is that even though the particles are spherical, the simplest way and a good first examination is to zoom into the interface closely enough that the curvature of the interface can be considered a plane. The interface of the plane is located at z=0. The metal has a complex

dielectric constant ϵ_1, with ϵ_1' being the real part, and ϵ_1" being the imaginary part. The other medium, which could be glass, air, or a solution, has a different dielectric constant ϵ_2.

In order to model these surface plasmon resonances and their properties, it is necessary to first start by finding homogeneous solutions to Maxwell's equation [24]:

$$\nabla \times \nabla \times \mathbf{E}(\mathbf{r},\omega) \; - \; \frac{\omega^2}{c^2}\varepsilon(\mathbf{r},\omega)\,\mathbf{E}(\mathbf{r},\omega) \; = \; 0 \qquad (13)$$

Brongersma goes through how to find the solution to this equation in rigorous detail. However, it turns out that solutions to this equation only exist when the following conditions are satisfied [23]:

$$\begin{aligned} \varepsilon_1(\omega)\cdot\varepsilon_2(\omega) &< 0 \\ \varepsilon_1(\omega)+\varepsilon_2(\omega) &< 0 \end{aligned} \qquad (14)$$

This condition implies that the real part of the dielectric constant of one of the mediums must be negative with an absolute value that is greater than the dielectric constant of the second medium. Since metals often possess a large negative dielectric constant, they are the typical materials used to study surface plasmon resonances. More importantly, after solving this equation the wavevector k of the surface plasmon is found to be given by [23]:

$$k'_{\mathrm{x}} \;\approx\; \sqrt{\frac{\varepsilon'_1\varepsilon_2}{\varepsilon'_1+\varepsilon_2}}\frac{\omega}{c} \qquad (15)$$

$$k_x'' \approx \sqrt{\frac{\varepsilon_1' \varepsilon_2}{\varepsilon_1' + \varepsilon_2}} \frac{\varepsilon_1'' \varepsilon_2}{2\varepsilon_1'(\varepsilon_1' + \varepsilon_2)} \frac{\omega}{c} \quad (16)$$

$$k_{1,z} = \frac{\omega}{c} \sqrt{\frac{\varepsilon_1'^2}{\varepsilon_1' + \varepsilon_2}} \left[1 + i \frac{\varepsilon_1''}{2\varepsilon_1'}\right] \quad (17)$$

$$k_{2,z} = \frac{\omega}{c} \sqrt{\frac{\varepsilon_2^2}{\varepsilon_1' + \varepsilon_2}} \left[1 - i \frac{\varepsilon_1''}{2(\varepsilon_1' + \varepsilon_2)}\right] \quad (18)$$

where k_x is the wavevector of the surface plasmon resonance travelling longitudinally along the interface, with a real component k'_x and an imaginary component $k"_x$. $k_{1,z}$ and $k_{2,z}$ are the transverse wavevectors travelling in the metal and glass respectively. Within these equations, ω is the frequency of the applied electric field, and c is the speed of light in vacuum. These wavevectors can then be used to calculate the decay length of the surface plasmon resonance through either medium. The decay length of the longitudinal plasmon propagation along the interface is given by 1/2 $k"_x$, the decay length of the transverse plasmon propagation in metal is given by $1/k_{1,z}$, and the decay length of transverse plasmon propagation in the second medium is $1/k_{2,z}$. By definition, the decay length, regardless of the direction or medium, is the distance at which the strength of the surface plasmon resonance electric field has decayed by 1/e. Figure 24 illustrates a surface plasmon generated from a metal-air interface along with its various decay lengths [23].

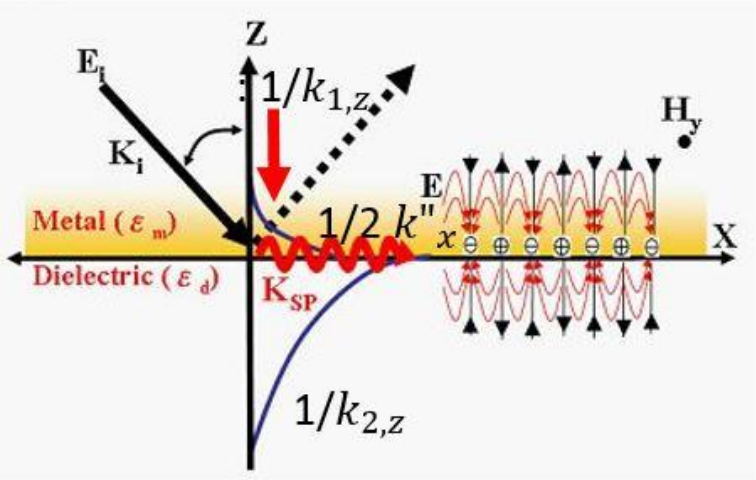

Figure 24: *A cartoon illustrating how an incoming electric field generates a surface plasmon. Once generated, the surface plasmon decays longitudinally by $1/2k''_x$ and decays transversely by $1/k_z$.*

In order to be able to strongly detect a surface plasmon resonance effect, the depth of the metal surface must be less than the decay length. If the depth is larger, than any surface plasmons that are generated will be absorbed by the material. In the instance of in-fiber particles, the particle diameter must be smaller than the transverse decay length in the metal. When the appropriate parameters are plugged into the above equations [25-26], in order to observe surface plasmonic resonances from a Silver sphere embedded inside of a silica fiber in the visible spectrum (for example, to see a plasmonic resonance peak at about 630 nm), the Silver particle size must be smaller than 20 nm. At the time that this thesis was written, fabricating in-fiber particles of that size through the capillary instability break up method was still quite a feat. However, if instead we were looking for a plasmonic resonance peak in the terahertz regime, the Silver particle size must be between 1 um (for a 1 Thz peak) to 10 um (for

a 0.2 Thz peak). Particles with this diameter have been achieved in the past [3], which is a promising result for seeking terahertz plasmonic resonances from this system.

4.2 Terahertz Plasmonic Effects in Silver Microspheres

A Silver redrawn fiber (core size: 7 um) underwent the capillary break up process to generate an in-fiber array of spheres with a diameter of 30 um. These spheres were then taken to a Terahertz Time Domain Spectroscopy (Thz-TDS) set up in order to measure the transmission spectrum of these fibers in the terahertz regime. Figure 25 shows the sample holder for this Thz-TDS experiment. First, two fibers without any core material (ie glass only) were placed over the two apertures. Thz-TDS measurements were then taken on this sample in order to obtain a reference spectrum, which can be seen in Figure 26. Since there is no difference between the resulting curve from aperture 1 and aperture 2, it can be seen that there is no experimental difference between the two apertures. This allows for two different samples to be placed on the sample holder, thus allowing the need for only one measurement to compare two different samples.

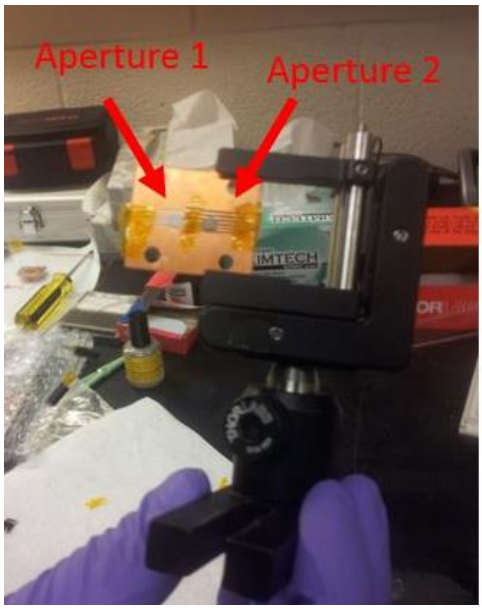

Figure 25: *A picture of the sample holder used to conduct the Thz-TDS experiments.*

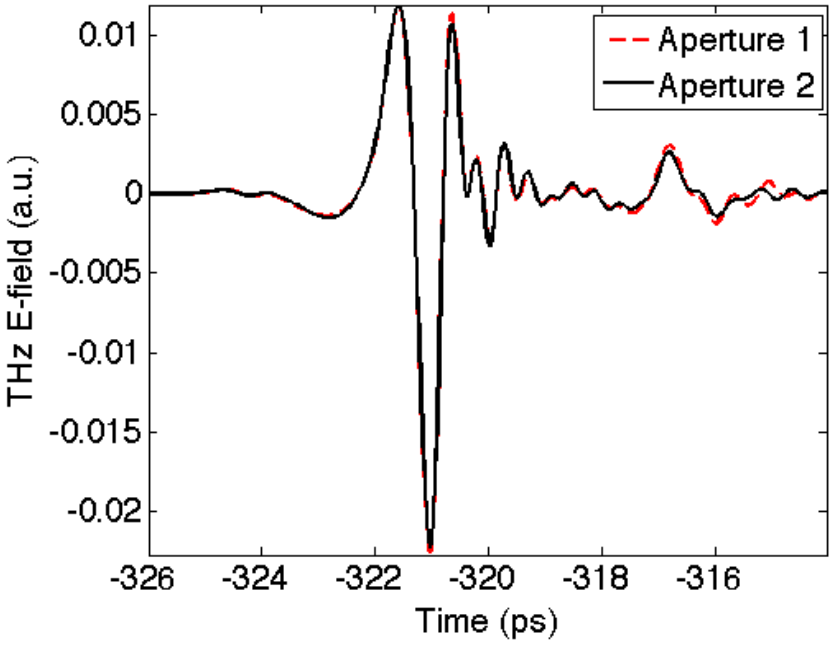

Figure 26: *A reference Thz-TDS spectrum. This curve shows tracks a terahertz pulse over time.*

In the following experiment, a fiber with just a Silver core was placed over Aperture 1, while a fiber with the Silver microspheres was placed over Aperture 2. The resulting spectrum can be seen in Figure 27. Instead of seeing a resonance peak from the spheres around 1 Thz, the terahertz transmission is instead diminished. This is most likely due to there being more available glass in the sample than in the core sample, and the glass is most likely absorbing some of the terahertz radiation. In addition, since these particle sizes were theoretically too large to observe plasmonic effects to begin with (30 um instead of the desired 10 um), it is understandable that plasmonic effects were not observed. In order to observe these effects, more effort needs to be put into successfully tapering a redrawn Silver fiber down to a core size of about 700-800 nm. From there, when the capillary break up step occurs, the resulting Silver particle size would be around the desired size of 10 um.

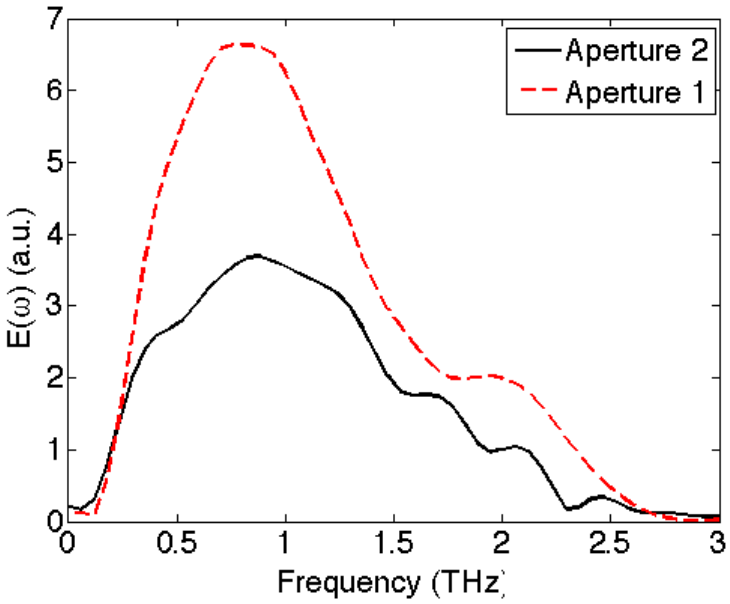

Figure 27: *The Thz transmission spectrum. Aperture 1 contains glass only, Aperture 2 contains the spheres.*

Summary

Not only do fibers allow for materials to be fabricated with a microscale diameter and on a length scale of meters, but by taking advantage of the fluidic phenomenon of capillary instability, tunable in-fiber micron sized particles can be generated. These fiber encapsulated particles form a very unique system where novel phenomenon can be observed. For the case of semiconducting spheres, such as Germanium, solidification after the formation of these particles leads to a stress generation of 1.8 GPa, which can be observed by the measurement of a shift in its band gap energies. This experimentally observed pressure is in agreement with theory. Other members of our lab have examined this stress generation in other materials, and is currently working on ways to exploit this pressure generation in a practical application. For the case of metallic spheres, such as Silver, it is possible to observe a terahertz plasmonic resonance in these in-fiber spheres. However, the current break up instrument is not able to consistently produce Silver spheres at the necessary size for a plasmonic resonance peak to be observed. However, once the break up instrument has been optimized to handle fibers of such a small diameter, plasmonic resonances in the terahertz regime will be able to be observed, and further applications of this resonance will be able to be explored.

References

[1] S. Garner, S. Glaesemann, X. Li. “Ultra-slim flexible glass for roll to roll electronic device fabrication”. *Applied Physics A. Materials Science and Processing,* 116, 403-7, 2014.

[2] A.F. Abouraddy, M. Bayindir, G. Benoit, S.D. Hart, K. Kuriki, N. Orf, O. Shapira, F. Sorin, B. Temelkuran, Y. Fink. “Towards multimaterial multifunctional fibres that see, hear, sense, and communicate”. *Nature Review*, 6, 336-47, 2007.

[3] A. Gumennik, L. Wei, G. Lestoquoy, A. Stolyarov, X. Jia, P. Rekemeyer, M. Smith, X. Liang, B. Grena, S. Johnson, S. Gradecak, A. Abouraddy, J. Joannopoulos, Y. Fink. “Silicon-in-silica spheres via axial thermal gradient in-fibre capillary instabilities”. *Nature Communications,* 4, 2216-25, 2013.

[4] S. Shabahang, J. Kaufman, D. Deng, A.F. Abouraddy. “Observation of the Plateau-Rayleigh capillary instability in multi-material optical fibers”. *Applied Physics Letters*, 99, 16-21, 2011.

[5] J. Xu, L. Zhang, Q. Guo, S. Zhou, C. Feng. “Research on the preparation of antimony nanoparticles by mechanical ball milling”. *Key Engineering Materials*, 609, 244-9, 2014.

[6] J. Wu, X. Zan, S. :I, Y. Liu, C. Cui, B. Zou, W. Zhang, H. Xu, H. Duan, D. Tian, W. Huang, F. Huo. “In site synthesis of large-area single sub-10 nm nanoparticle arrays by polymer pen lithography”. *Nanoscale*, 6, 749-52, 2014.

[7] D. Deng, J. Nave, X. Liang, S. Johnson, Y. Fink. “Exploration of in-fiber nanostructures from capillary instability”. *Optics Express*, 19, 16273-90, 2011.

[8] J. Strutt, “On the instability of jets”, *Proceedings of the London Mathematical Society*, 10, 4-13, 1878.

[9] K. Kaufman, G. Tao, S. Shabahang, E. Banaei, D. Deng, X. Liang, S. Johnson, Y. Fink, A. Abouraddy. “Structured spheres generated by an in-fibre fluid instability”. *Nature Letters*, 487, 463-7, 2012.

[10] S. Tomotika. “On the instability of a cylindrical thread of a viscous liquid surrounded by another viscous fluid”. *Proceedings of the Royal Society*, 150, 322-39, 1935.

[11] M. Assael, A. Kalyva, K. Antoniadis, R. Banish, I. Egry, J. Wu, E. Kaschnitz, W. Wakeham. “Reference data for the density and viscosity of liquid antimony, bismuth, lead, nickel and silver”. *High Temperatures-High Pressures*, 41, 161-84, 2012.

[12] S. Little, A. Begou, T. Collins, R. Marsillac. “Optical detection of melting point depression for silver nanoparticles via in situ real time spectroscopic ellipsometry”. *Applied Physics Letters*, 100, 34-9, 2012.

[13] J. Eshelby. “The Determination of the Elastic Field of an Ellipsoidal Inclusion and Related Problems”. Proceedings of the Royal Society of London, **Ser. A**, A241, 376–396, 1957.

[14] C. Ekuma, M. Jarrell, J. Moreno, D. Bagayoko. “Re-examining the electronic structure of germanium: A first-principle study”. *Physics Letters A*, 377, 2172-76, 2013.

[15] J. Williams, B. Harber, S. Deshmukh, B. Johnson, B. Malone, M. Cohen, J. Bradby. “Hexagonal germanium formed via a pressure-induced phase transformation of amorphous germanium under controlled nanoindentation” *Physica Status Solidi-Rapid Research Letters*, 7, 355-9, 2013.

[16] H. Zhou, L. Ge. “Investigation on the shear moduli and damping ratios of silica gel”. *Granular Matter*, 16, 449-56, 2014.

[17] E. Kurdi, G. Fishman, S. Sauvage, P. Boucaud. “Band structure and optical gain of tensile-strained germanium based on a 30 band k p formalism”. *Journal of Applied Physics*, 107, 10-17, 2010.

[18] E. Ghahramani, J. Sipe. “Pressure dependence of the band gaps of the semiconductors”, *Physics Review B,* 40, 12516 – 12519, 1989.

[19] A. Goni, K. Syassen, M. Cardona. “Direct-band-gap absorption in germanium under

pressure”, *Physics Review B,* 39, 12921-12924, 1989.

[20] M. Misra, Y. Pan, C. Williams, S. Maier, S. Andrews. “Characterization of a hollow core fibre-coupled near field terahertz probe”. *Journal of Applied Physics*, 113, 104-15, 2013.

[21] A. Angeluts, M. Nazarov, A. Yu. Ryabov, D. Pebalk, A.P. Shkurinov. “Surface Plasmon Propagation on a film with subwavelength holes in the terahertz frequency range”. *Radiophysics and Quantum Electronics,* 55, 634-49, 2013.

[22] N. Yu, Q. Wang, M. Kats, J. Fan, F. Capasso, S. Khanna, L. Li, A. Davies, E. Linfield. “Terahertz plasmonics”. *Electronics Letters*, 10, s52-s57, 2010.

[23] M. Brongersma, P. Kik. “Surface Plasmon Nanophotonics”. Springer, 2007.

[24] Y. Oijala, J. Markkanen, S. Jarvenpaa, P. Sami. “Surface and Volume Integral Equation Methods for Time-Harmonic Solutions of Maxwell’s Equations”. *Progress in Electromagnetics Research*, 149, 15-44, 2014.

[25] A. Rusina, M. Durach, M. Stockman. “Theory of spoof plasmons in real metals”. *Applied Physics A*, 10, 5866-870, 2010.

[26] A. Kumbhar, M. Kinnan, G. Chumanov. “Multipole Plasmon Resonances of Submicron Silver Particles”. *Journal of the American Chemical Society*, 127, 12444-12445, 2005.